# Quantum correlation imaging via X-ray parametric down-conversion

JUSTIN C. GOODRICH[1,*], RYAN MAHON[1], JOSEPH HANRAHAN[1], DENNIS BOLLWEG[2,†], MONIKA DZIUBELSKI[3], RAPHAEL A. ABRAHAO[3,‡], SANJIT KARMAKAR[4], KAZIMIERZ J. GOFRON[5], THOMAS A. CASWELL[1], DANIEL ALLAN[1], LONNY BERMAN[1], ANDREI NOMEROTSKI[6,7], ANDREI FLUERASU[1], CINZIA DAVIÀ[4,8], SEAN MCSWEENEY[1,9]

[1]*National Synchrotron Light Source II, Brookhaven National Laboratory, Upton, NY 11973, USA*
[2]*Computing and Data Sciences Directorate, Brookhaven National Laboratory, Upton, NY 11973, USA*
[3]*Physics Department, Brookhaven National Laboratory, Upton, NY 11973, USA*
[4]*Department of Physics and Astronomy, Stony Brook University, Stony Brook, NY 11790, USA*
[5]*Spallation Neutron Source, Oak Ridge National Laboratory, Oak Ridge, TN 37831, USA*
[6]*Department of Electrical and Computer Engineering, Florida International University, Miami, FL 33174, USA*
[7]*Faculty of Nuclear Sciences and Physical Engineering, Czech Technical University in Prague, 11519 Prague, Czech Republic*
[8]*Department of Physics and Astronomy, The University of Manchester, Manchester M13 9PL, UK*
[9]*Biology Department, Brookhaven National Laboratory, Upton, NY 11973, USA*
[†]*Current address: Flatiron Institute, Simons Foundation, New York, New York 10010, USA*
[‡]*Current address: School of Physics and Astronomy, Center for Detectors, Future Photon Initiative, Rochester Institute of Technology, Rochester, New York 14623, USA*
[*]*jgoodrich@bnl.gov*

**Abstract:** Quantum imaging leverages correlations between pairs of photons and has the potential to obtain image information beyond what classical sources provide. Extending this approach to the X-ray regime has been limited by low photon-pair generation rates and the lack of suitable detectors. Here, we demonstrate X-ray coincidence imaging using spontaneous parametric down-conversion (SPDC) and a pixelated area detector with time- and energy-resolved capabilities. This configuration enables simultaneous detection of correlated X-ray photon pairs and coincidence-based imaging of test objects, including a biological specimen. The increased coincidence rate and spatially resolved detection establish a basis for future quantum-enhanced and low-dose X-ray imaging.

## 1. Introduction

The generation, manipulation, and detection of single photons has led to numerous advancements in quantum information science and technology. Spontaneous parametric down-conversion (SPDC) is a key method for producing pairs of correlated single photons [1–4]. SPDC is a transformative technique used in both fundamental quantum physics [5–8] and various quantum technologies [9–14]. During the SPDC process, a photon from a pump beam is down-converted in a non-linear material into a pair of correlated photons, commonly called the signal and idler. This process has been widely applied in the visible and infrared spectral regimes. However, adapting this method to X-ray energies poses significant challenges, including the low conversion efficiency of commonly used media, such as single crystal diamond, and the absence of rapid, energy-resolving X-ray detectors [15–31].

In this study, we report new insights into both the theoretical and experimental aspects of X-ray SPDC. We performed quantum correlation imaging (twin-imaging) of various objects, including a structurally complex biological sample (E. cardamomum seed), using X-ray SPDC

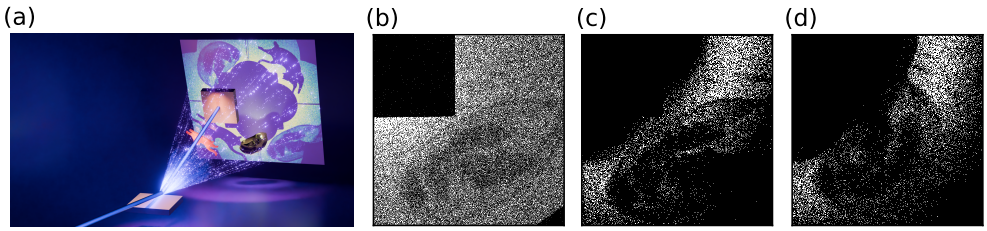


Fig. 1. Quantum X-ray correlation imaging. (a) A conceptual schematic of the non-linear X-ray diffraction (SPDC) imaging setup. 15 keV pump X-rays from a synchrotron light source produce a ring of SPDC biphotons resulting from the non-linear diffraction of a diamond crystal. Imaging objects, including a patterned tungsten test object (cat-shaped) and an E. cardamomum seed, are placed within the ring on the lower two chips of the detector, while the upper chips remain unobstructed. Coincidence measurements yield twin images, one in the signal plane (lower chips) and one deformed due to energy non-degeneracy in the idler plane (upper chips). (b) Reference image of the cardamom seed captured using a classical light source of scattered 15 keV pump X-rays. (c) The quantum correlation image of the seed on the signal plane with photon energies probing the samples ranging from 5 to 10 keV. (d) The quantum correlation twin image of the seed on the idler plane, rotated to align with the signal detector's frame of reference for easier comparison, showing distortion due to the non-degeneracy of the X-ray photon pairs. Figures (b)-(d) were generated using the same number of photons for accurate comparison.

photon pairs detected at rates approximately 25 times higher than previously reported synchrotron values [29] and approximately six times higher than recently reported at an XFEL [30]. We also investigated the influence of the crystalline quality of the non-linear medium and beam divergence on the properties of the generated biphotons. Furthermore, we discuss the prospects of using such correlated photons for quantum-enhanced transmission measurements, including sub-shot-noise imaging modalities. These results demonstrate the practical feasibility of using quantum correlations for X-ray radiography, representing an important step toward reducing radiation exposure in dose-sensitive materials [32, 33]. Compared with earlier demonstrations using one-dimensional detectors [31], this work extends such approaches through high-throughput detection with area detectors and the first demonstration of X-ray coincidence imaging of a biological sample. Together with related studies exploring nonclassical and correlation-based imaging modalities in the optical regime [14, 34–39], our findings clarify the feasibility and broader significance of quantum X-ray methods for both applied imaging and fundamental studies in quantum optics.

## 2. X-ray Quantum Correlation Imaging

Quantum imaging offers significant advantages over classical imaging in several metrics [14,40,41]. These include super-resolution capabilities that surpass the Rayleigh diffraction limit [37, 42, 43], noise reduction by measuring signals only coincident in two independent detection systems [12,38], and an enhanced signal-to-noise ratio (SNR) in transmission imaging under ultra-low light levels by correlating the so-called signal and idler photon coincidence counts (sub-shot-noise imaging) [39, 44, 45]. Despite significant advances in the optical regime, to date these techniques have remained largely inaccessible in the X-ray regime owing to the aforementioned challenges in the generation and detection of a sufficient number of correlated X-ray pairs.

In our proof-of-concept experiment of imaging complex biological samples, we utilized the simultaneous detection of X-ray biphotons with a high-speed, two-dimensional pixelated area

detector. This setup enabled the production of quantum correlation radiographs of various objects, including the intricate biological structure of an E. cardamomum seedpod. To the best of our knowledge, this is the first demonstration of quantum correlation X-ray imaging on a biological specimen.

As illustrated in the conceptual schematic describing the experiment (Fig. 1a), the characteristic ring generated by the correlated SPDC photon pairs is recorded by a Lynx T3 pixelated area detector, which consists of four Timepix3 silicon ASICs. The top two chips are used to detect idler photons that are unobstructed by the objects under study, whereas the bottom two chips detect signal photons on the paths of the objects. By correlating coincident photon events in both detector arms, we generated two distinct quantum images, each from the respective frame of reference of the detectors (signal and idler, respectively). Fig. 1b-d show images of the cardamom seed using a classical source (scattered pump X-rays from the diamond crystal), as well as the quantum images with comparable photon counts. The image distortion (Fig. 1d) is due to the presence of non-degenerate pairs, which distribute on the ring non-linearly to satisfy conservation of momentum. The use of quantum correlations has the inherent property of reducing detector noise, as any electronic noise or cosmic rays incident on the sensor would have to exist simultaneously in both the signal and idler arms to be marked as coincident. On the other hand, other sources of noise, such as those from the scattered background, are always present because their arrival time is within the time resolution of the detector, and therefore require a more sophisticated pair-selection process. The improved detection capability of non-correlated single photons will reduce the uncertainty of the number of incident photons for projection imaging, which is useful for roentgenography and computed tomography measurements with significantly reduced doses [39].

## 3. Generation and Identification of X-ray SPDC

The SPDC process occurs if conservation of energy and conservation of momentum are satisfied, the latter commonly called phase matching. In our case, phase matching for X-ray down-conversion occurs when the crystal is detuned very slightly from the Bragg condition [15–17, 20]. The extremely low SPDC conversion efficiency of $<10^{-10}$ significantly limits the number of generated photon pairs compared to similar processes in the optical regime. This difficulty is exacerbated by the substantial background of scattered pump photons that also reach the detector. The Timepix detector technology measures two additional timing parameters along with the (x, y) pixel coordinate of an event: the time-of-arrival (ToA) with 1.5625 ns precision, and the time-over-threshold (ToT) with 25 ns precision. The former allows us to time-stamp detection events for coincidence detection, while the latter acts as a proxy for the measurement of the energy of the detected photon. These two parameters facilitate the pairing of photons based on the smallest time differences after filtering out high-energy background events. Selecting such events allows for the detection of photon pairs with strongly correlated emission angles emerging from the diamond crystal and a robust time coincidence signal. Although the time precision of the Timepix3 chip is 1.5625 ns, the "timewalk" phenonemon [46, 47], along with variations in the X-ray conversion points in the silicon detector, results in an effective time resolution on the order of ~20 ns. Further refinement of the selected events based on spatial properties, such as pairs that are seen to conserve both the diffracted pump energy and momentum, allows for the isolation of SPDC photon pairs with high SNR (>100) [48].

In our experiments, the detuning angle was set to 0.040°, which was chosen to position the half-energy ring on the detector between the detector edges and a tungsten beamstop, which blocks the direct Bragg reflection. Despite the detuning angle being locked in such a way, the SPDC photon pairs were measured to have a spread of emission angles $\alpha_s$ and $\alpha_i$ on the order of 0.1° (Fig. 2a). It is possible to compute the value of the detuning angle from each measured pair by applying the energy conservation law and knowing the existing inverse relationship between

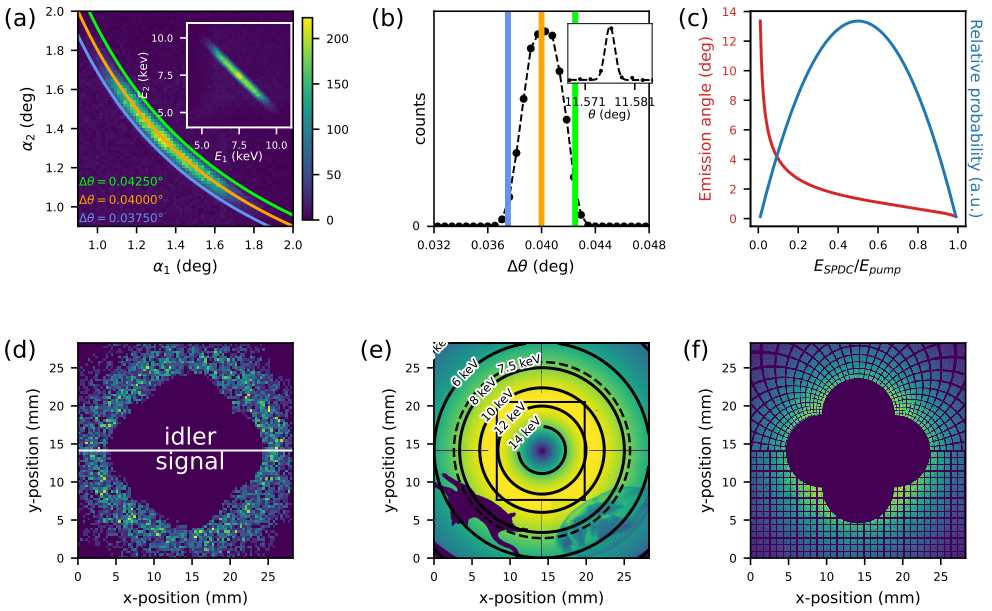


Fig. 2. X-ray SPDC Properties. (a) Calculated emission angles and photon energies (inset) of isolated SPDC single photons align with theoretical phase-matching predictions, confirming energy conservation and non-degeneracy. Data from 38 hours with imaging mask obstructing the detector. (b) Pair detuning angles, derived from emission angles, show a spread around the nominal 0.040°, correlated with crystalline misorientation, beam divergence, and Darwin width (rocking curve inset). Same dataset as (a). (c) Radial distances and relative probabilities of SPDC photons vs. angle. (d) Measured positions of correlated pairs in a characteristic ring pattern from a single exposure. Lossy regions occur when one photon falls outside the detector. The detector is split into a signal region and an idler region. Ghost images appear on the idler detector when images are placed to occlude the signal detector. (e) SPDC energy contours and occupation density with a quantum correlation imaging mask (tungsten cat and E. cardamomum seedpod). (f) A square grid on the signal detector (bottom) maps onto circular contours on the idler detector (top) due to non-degenerate energy correlations.

the energy and emission angle for each photon (see Supplemental Information for derivation):

$$\Delta\theta = \frac{\alpha_s \alpha_i}{2\sin(2\theta)} \tag{1}$$

This calculation suggests that SPDC photons are generated with a spread of detuning angles, centered around the preset angle with a standard deviation ($\sigma$) of 0.0014° (Fig. 2b). The observed variance in the detuning angle corresponds to the variance of the measured diamond (111) Bragg peak rocking curve during the crystal alignment. For reference, the Darwin width of the diamond (111) Bragg reflection at 15 keV is 0.75 mdeg, of the upstream Si (111) monochromator Bragg reflection is 1 mdeg, and the vertical divergence of the incident beam, taking account of the source and slit sizes and distance separating them, was 0.1 mdeg. Compared with the measured rocking curve (full width at half max) FWHM of 3 mdeg, the crystal mosaicity is the predominant contributor to the rocking curve width. This correlation provides strong evidence that the mosaicity of the crystal, along with beam divergence, influences the phase matching of the SPDC process in a way comparable to the effect of such influences when performing $\theta$ scans (rocking curves). Furthermore, it indicates the importance of minimizing beam divergence and

using a high quality non-linear medium for the generation of robust X-ray photon pairs; achieving the latter, for a diamond crystal, entails using as perfect a crystal as possible with a minimum of mosaicity.

The final selections indicate SPDC rates approaching $7.8 \times 10^3$ pairs per hour, significantly surpassing previous benchmarks reported in the literature [29]. This is primarily attributed to the improved detector performance; the large, pixelated detection area (2.8 cm by 2.8 cm) significantly improves the solid angle coverage in comparison to previous studies which used silicon drift detectors and the event-driven mode providing spatial, temporal, and energy information for each hit provides more information per photon than previous detector technologies. Other factors include the high brightness of the 11-ID Coherent Hard X-ray Scattering (CHX) beamline and optimization of the chosen detuning angle to our experimental setup (detector distance and acceptance) in order to capture the maximum number of coincidences. Detecting pairs at this rate with a two-dimensional area detector (Fig. 2d) substantiates the practicality of utilizing the X-ray SPDC source for quantum imaging experiments, which was previously limited due to low count rates and the utilization of slit-based detectors [31]. Additionally, identifying the spread of detuning angles sheds light on the influence of the pump and diamond properties on the generation of SPDC biphotons. This understanding facilitates the use of sharpening corrections for the image blurring which arises from the spread of the pair emission angles. Such corrections can enhance the image clarity and precision while providing important insights into the best pump characteristics, crystalline quality, and detuning angles necessary for the production of SPDC pairs with minimal emission angle dispersion.

## 4. SPDC Photon Energy and Spatial Properties

A complete understanding of the energy and spatial properties of X-ray SPDC sources is essential for their successful application in quantum imaging. The SPDC process generates correlated single photons over a broad energy spectrum, which is given by the probability [16]:

$$\eta(E_{SPDC}) \propto E_{SPDC}(E_{pump} - E_{SPDC}) \tag{2}$$

where $E_{SPDC}$ is the energy of an SPDC photon and $E_{pump}$ is the energy of the X-ray pump. The highest probability of generating an SPDC pair occurs at degeneracy, where $E_{signal} = E_{idler} = \frac{1}{2}E_{pump}$. However, a significant number of photons are generated in non-degenerate conditions. The angle between the wave vector $\mathbf{k}_{SPDC}$ and the diffracted pump $\mathbf{k}_{out}$ is given by the function $\alpha(b)$, where b = $\frac{E_{SPDC}}{E_{pump}}$. The distance $r$ between the SPDC photon and the diffracted pump on the detector is given by:

$$r = L\tan(\alpha(b)) \tag{3}$$

where $L$ is the distance between the detector and the diamond crystal. Considering the phase matching condition and conservation of momentum, with some approximations (see Supplemental Information) one can relate the energy of a photon with its position using the following equation:

$$E_{SPDC}(r) \approx \frac{E_{pump}}{\frac{\arctan^2(\frac{r}{L})}{2\Delta\theta sin(2\theta)} + 1} \tag{4}$$

Based on Equations 2 and 4, we derive the expected photon occupation and spatial distance as a function of the single photon energy fraction $b$ (Fig. 2c). The detected degenerate and non-degenerate photon pairs distribute on precisely defined energy rings, allowing the sample under study to be exposed to different X-ray energies over its cross sectional area, depending on the momentum transfer vector (Fig. 2c,e). A down-converted photon detected at position

$(x, y)$ with a radial distance $r$ from the diffraction center will have its idler counterpart incident at position $(x', y')$ with radial distance $r'$ given by:

$$r' \approx L \tan\left(\frac{2\Delta\theta \sin(2\theta)}{\arctan\left(\frac{r}{L}\right)}\right) \approx \frac{\tan\left(\sqrt{2\Delta\theta \sin(2\theta)\frac{b}{1-b}}\right)}{\tan\left(\sqrt{2\Delta\theta \sin(2\theta)\frac{1-b}{b}}\right)} \tag{5}$$

The effect of this mapping is demonstrated in Fig. 2f, where an image of a square grid on the signal detector is twinned as circular contours on the idler detector.

The non-degenerate properties of the source indicate the possibility of engineering a system to perform lensless geometric magnification by correlating high energy X-rays probing a sample with their lower energy counterparts at steeper emission angles. It also suggests the capability of an imaging mechanism in which the detuning angle is swept across a range of angles, exposing the samples to different energies over time, allowing for quantum X-ray absorption and quantum fluorescence spectroscopy schemes.

## 5. Spatial Correlations and Detuning Corrections

A key property of the X-ray quantum signal and idler correlation images (Fig. 3a) is their dual mirroring and flipping relationship. This can be most clearly observed with the cat-shaped test object, whose head is positioned on the inner side of the ring on the signal detector (lower left quadrant), appearing on the outer part of the ring in the idler detector (upper right quadrant). Similarly, the cardamom seed projects a direct image on outer ring radii, which are mirrored and flipped on the idler detector onto inner radii near the beam stop. This effect is due to the correlation of low emission angle, higher energy X-rays being absorbed by the objects being correlated with steeper emission angle, lower energy X-rays. In addition, the mapping of straight segments into circular contours is due to the energy non-degeneracy. The effect of this transformation becomes more significant when the object is positioned further away from the degenerate energy ring.

Furthermore, an aberration is present in the twinned correlation images because biphotons are generated with a spread of detuning angles. This indicates the necessity of minimizing the pump divergence, using a high quality single crystal medium, and maximizing the detuning angle in order to reduce the impact of $\frac{\sigma_\theta}{\Delta\theta}$, i.e. the ratio of the rocking curve width ($\sigma_\theta$) to the detuning angle ($\Delta\theta$). However, increasing the detuning angle leads to other trade-offs: the emission angles of the biphotons increase, which requires either a larger detector while maintaining the detector distance or moving the detector closer to the diamond, thus sacrificing the effective resolution.

One possible approach to correct this blurring is to scale the radial distances of events on the idler detector to distances that would have resulted from the nominal detuning angle (Fig. 3b) via a form factor expressed by the ratio $\frac{\theta_{nominal}}{\theta_{calculated}}$:

$$r'_{corrected} = L \tan\left(\frac{\Delta\theta_{nominal}}{\Delta\theta_{calculated}}\alpha'\right) \tag{6}$$

This sharpening correction applies a deterministic scaling to all idler events based on the calculated detuning angle via Equation 1. The form factor represents a geometric correction derived from the experimentally determined detuning-angle spread. Simulations (Fig. 3c,d) of the detuning angle spread matched well with the experimental data and verified the utility of the correction Equation 6. The simulated correlation image in Fig. 3c was generated by introducing Gaussian-distributed angular deviations ($\sigma = 0.0014°$) to the calculated emission directions of each photon pair, reproducing the experimentally observed spread due to crystal mosaicity (Fig.

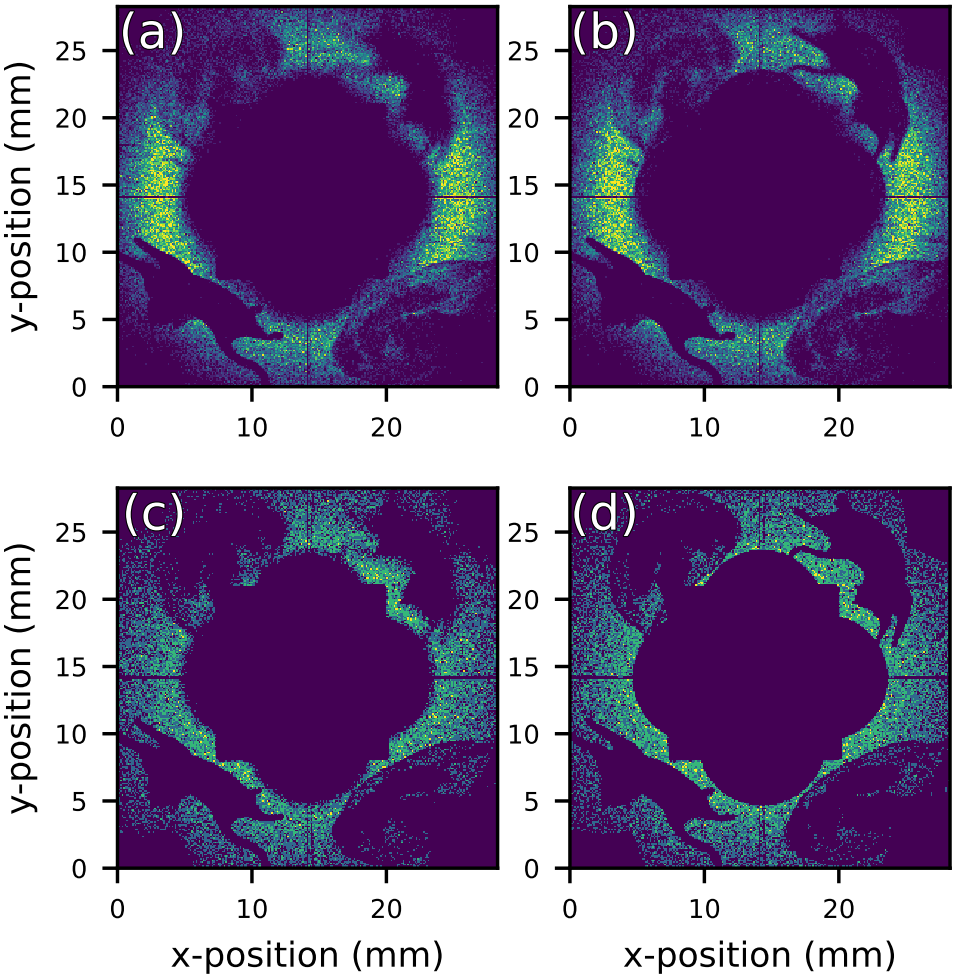


Fig. 3. X-ray correlation imaging simulations and experimental data. (a) Experimental X-ray correlation image before correction (38 hour exposure). (b) Experimental data after applying corrections from Equation 6 to photons on the top (idler) detectors. (c) Simulated X-ray correlation image with the SPDC detuning angles following a normal distribution centered at 0.040° with a standard deviation ($\sigma$) of 0.0014°. (d) Simulated correlation image with the SPDC detuning angle fixed at 0.040°.

3a). The SPDC correlation images clearly illustrate the distinct ring pattern characteristic of the spatial correlations between the X-ray photon pairs. This pattern is a direct manifestation of the quantum mechanical nature of photon pairs and validates the theoretical predictions of the SPDC X-ray properties. The ring pattern observed includes regions where the correlation is lost because one of the single photons is off the plane of the detector or occluded by the beamstop. This reveals the importance of controlling the experimental parameters (detector size, distance to the detector, and detuning angle) in efficient photon pair detection. Differences in image quality between corrected experimental and simulated data indicate the presence of other noise sources which could not escape the limited time and the spatial resolution of the detection system.

## 6. Towards Sub-shot-noise Transmission Imaging

One of the goals of the quantum imaging scheme presented herein is to demonstrate sub-shot-noise imaging. Sub-shot-noise imaging refers to reducing the noise below the shot-noise limit, which is determined by the Poissonian statistics of classical light sources [39, 44]. In traditional transmission imaging, photon statistics inherently follow a Poisson distribution, introducing uncertainty in the number of photons incident on the detector.

Consider imaging with a mean photon flux $\lambda$ per pixel. In a classical imaging scheme, the number of photons ($k$) detected in a pixel follows a Poisson distribution where the standard deviation is $\sqrt{\lambda}$. This statistical uncertainty leads to variability in the measured transmission, defined as:

$$t = \frac{N_{\text{measured}}}{N_{\text{incident}}}, \tag{7}$$

where $N_{\text{measured}}$ is the number of photons detected after the sample, and $N_{\text{incident}}$ is the number of photons incident on the sample. In classical imaging, $N_{\text{incident}}$ is approximated as the mean value $\lambda$ of the incident photon distribution. However, at low photon counts, the relative uncertainty in $N_{\text{incident}}$, given by $\frac{\sqrt{\lambda}}{\lambda}$, becomes significant. This high uncertainty degrades the signal-to-noise ratio (SNR) and necessitates the use of a larger photon dose to achieve reliable transmission measurements, as the limit of the uncertainty approaches 0 as $\lambda$ grows large.

Quantum imaging addresses this limitation in the photon sparse regime by utilizing biphotons generated through spontaneous parametric down-conversion (SPDC). In this scheme, the perfect number correlation between the paired photons allows the direct measurement of $N_{\text{incident}}$ in the reference arm, significantly reducing the resulting uncertainty in $t$. The joint distribution exhibits sub-Poissonian covariance, reducing uncertainty in the inferred transmission [45]. This correlation underlies sub-shot-noise behavior observed in optical biphoton experiments [39]. This enables precise measurements, even in the low photon count regime, minimizing the dose delivered to the sample.

To perform such measurements, it is necessary to detect both coincident events, when paired photons are detected in the reference and test arms, and non-coincident events, which occur when a photon is absorbed or otherwise not transmitted through the sample. The accurate identification of SPDC photons versus background photons (e.g., diffusely scattered pump photons) is critical in this process. The ability to successfully classify SPDC photons versus the background depends on the energy resolution of the detector and the ratio of SPDC photons to background photons. For X-ray SPDC, achieving high energy resolution is challenging due to material limitations in current X-ray detector technologies, along with the large amount of background scattering produced in the non-linear diffraction process. Nevertheless, this capability is essential for effectively rejecting background events and achieving sub-shot-noise imaging in the X-ray regime.

A simple model using Bayesian probability (see Supplementary Information for detailed derivation) was developed to determine the capability of the detection system to identify single SPDC photons, as a function of the energy resolution and SNR of the down-converted and background photons. In this model, the aggregate likelihood of correctly identifying an SPDC photon as such is given by:

$$\mathcal{P}_{SPDC} = \int_0^\infty h(t) P(SPDC|t) dt \tag{8}$$

where $h(t)$ is the detector ToT spectra of the down-converted photons and $P(SPDC|t)$ is the conditional probability that a measured event with time-over-threshold $t$ is an SPDC photon, given by:

$$P(SPDC|t) = \frac{h(t)}{h(t) + \beta g_{15\text{ keV}}(t)} \tag{9}$$

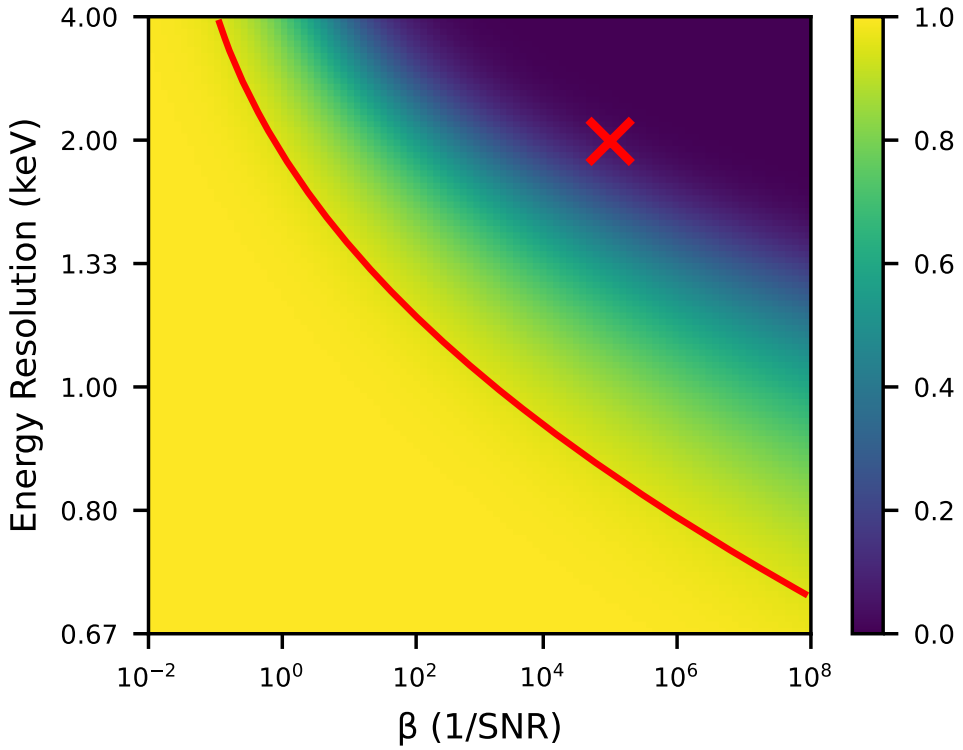


Fig. 4. SPDC Photon Identification Probability. The likelihood that an SPDC photon can be differentiated from a background photon as a function of the ratio of background events to down-converted events $\beta$ and the detector resolution, in keV. The red cross indicates the current measurements and the red contour line indicates where the likelihood of correct identification is 95%. Realistic improvements along both axes will allow for high-likelihood identification of SPDC photons against background, enabling advanced quantum imaging modalities such as sub-shot-noise imaging.

where $g_{15\,\mathrm{keV}}(t)$ is the ToT spectrum of the pump (15 keV) photons and $\beta$ is the ratio of background photons to SPDC photons on the detector. Both $h(t)$ and $g_{15\,\mathrm{keV}}(t)$ can also be functions of a resolution improvement factor $\zeta$, which impacts the standard deviations of the ToT spectra (e.g., $\sigma'_{ToT} = \sigma_{ToT}/\zeta$).

In our setup, the energy resolution is approximately 2 keV FWHM, with an SPDC-to-background photon ratio of the order of $\beta \approx 10^5$. Given these parameters and the pump photon energy of 15 keV, the numerical calculation of Equation 9 indicates an aggregate probability of approximately 4%. Modest improvements, such as improving the energy resolution by a factor of two ($\zeta = 2$) to 1 keV and reducing the background ratio by a couple orders of magnitude ($\beta \approx 10^3$), could increase the identification probability of single SPDC photons to over 95% (Fig. 4). Such enhancements appear feasible with advances in detector technology. For example, Timepix4 detectors, which are commonly known for their enhanced timing resolution, are also designed to achieve a twofold improvement in energy resolution (<1 keV FWHM) [49]. Additionally, the use of high-order crystalline reflections, such as (400) or (660) reflections at $2\theta$ angles approaching 90°, SPDC at the Brewster angle, and in Laue geometries, have been shown to significantly suppress background photons [26, 27, 29]. These improvements would enable precise SPDC

photon identification, a critical step for realizing sub-shot-noise imaging. We anticipate that these measurements will be achievable and plan to target them in future studies.

## 7. Conclusion

Our experimental investigation at the CHX beamline of the National Synchrotron Light Source II (NSLS-II) facility at Brookhaven National Laboratory (BNL) provided new data relevant to X-ray quantum imaging. Using a pixelated detector, we observed the characteristic ring pattern associated with SPDC and measured the spatial correlations of photon pairs at a rate of approximately $7.8 \times 10^3$ pairs per hour. This source was used to perform coincidence imaging of several test objects, including a biological sample (E. cardamomum seed pod). We analyzed the influence of crystalline imperfections and pump beam divergence on the properties of down-converted photons and introduced a correction procedure for related imaging aberrations. We also outlined the experimental conditions under which quantum-enhanced transmission (sub-shot-noise) measurements may become feasible, emphasizing the roles of the detector efficiency and background suppression.

This study contributes to the development of quantum imaging approaches with potential applications in contexts where minimizing the radiation dose is important, such as the study of radiation-sensitive biological materials. The increased detection rates of SPDC-generated X-ray photon pairs demonstrate the progress toward making quantum imaging techniques experimentally viable in the X-ray regime. Our implementation of quantum correlation imaging offers a basis for the further exploration of high-resolution and low-dose imaging strategies. The combination of measurements and simulations enhances our understanding of X-ray SPDC and informs ongoing efforts to optimize imaging system performance. These results enhance our understanding of quantum imaging at high-brightness X-ray sources, including synchrotrons and free-electron lasers.

## 8. Methods

### *8.1. Beamline Configuration*

Our investigations were conducted at the 11-ID CHX beamline of the NSLS-II facility at BNL. The beamline was configured to produce a monochromatic X-ray beam of 15.000 keV. The average input flux of the generated pump beam was approximately $10^{11}$ photons/second, with a polarization of 99% in the horizontal direction and $\frac{\Delta E}{E} \approx 10^{-4}$. The dimensions of the 15 keV input beam were set to 50 $\mu$m (horizontal) x 50 $\mu$m (vertical). Variabilities in flux rate over time can cause slightly different production rates. The double-crystal monochromator employed the Si (111) reflection, ensuring the absence of sub-harmonic (e.g., 5 keV) components that could arise from higher-order reflections such as Si (333). The beamline feedback and monitoring systems were monitored to ensure no significant deviation over the course of the experiment. The experiment used NSLS-II's standard continuous filling mode. The storage ring held ~500 mA of electrons in top-off mode with 1340 RF buckets, including 1000 filled buckets with approximately 2 ns between, and an ion clearing gap with a singlet bunch. This thereby limited the time resolution to the X-ray absorption depth and hole drift time in the silicon sensor of the detector.

### *8.2. Sample and Environment*

The incident X-ray beam was directed onto a (111) diamond single crystal with dimensions of 3 mm x 3 mm x 0.33 mm, grown by chemical vapor deposition from Element Six [50], which was used as the non-linear medium for the generation of correlated photon pairs. A vacuum-pumped flight path beam pipe was installed between the diamond crystal and the detector surface. The total path distance from the crystal to the detector surface was 49.4 cm. This distance was

confirmed from the scattering pattern of a standard SAXS distance calibration sample, silver behenate.

### 8.3. Sample Orientation

After the standard height alignment procedures, the diamond crystal was oriented to the (111) Bragg reflection at a Bragg ($\theta$) angle of 11.576°. Multiple vertical and lateral positions on the diamond were scanned to identify the region exhibiting the narrowest rocking-curve width, corresponding to minimal mosaicity. The resulting diffraction pattern peaked around a pixel coordinate of (260, 256) on a Lynx T3 (Timepix3) detector (by Amsterdam Scientific Instruments) which was subsequently employed to measure the SPDC signal.

A tungsten beamstop was strategically positioned to obscure the direct Bragg reflection and nearby scattering. The Bragg alignment was then fine-tuned with a deviation of ~0.040° to a $\theta$ angle of 11.618° to meet the phase matching condition. This adjustment instantiated the production of correlated X-ray pairs at a peak output angle of ~2.8°, an angle chosen to maximize the SPDC signal between the edge of the detector and the tungsten beamstop with the detector placed 68.3 cm away from the diamond at the $2\theta$ position.

### 8.4. Detector

To isolate the correlated X-ray photon pairs, we employed a Lynx T3 detector [51]. This detector combines four 256 x 256 pixel arrays of pixel size 55 x 55 $\mu$m, resulting in a total detector area of 512 x 512 pixels [52]. The top two chips were isolated for use as the “idler" detector whereas the bottom two chips were considered to be the “signal" detector for the quantum correlation imaging experiments. This detector was chosen for its accuracy in measuring time-of-arrival (ToA) and energy deposition (time-over-threshold or ToT). The two photons generated in the SPDC process should be coincident in time when reaching the detector. However, the signal amplitude dependence in the timestamping process results in a "timewalk" [46, 47], whereby events that arrive at the same time might measure a time difference of up to 100 ns. The time resolution could be further deteriorated by different time delays of ionization drift in silicon. This is due to the variation in the X-ray conversion points, because the absorption length of approximately 100 $\mu$m is of the same order as the sensor thickness of 300 $\mu$m. The measured resolution (rms) for the two X-rays time difference was ~18 ns. The detector was integrated into the control system of the CHX beamline through the development of an appropriate EPICS areaDetector driver [53–55] and Python objects for integration with the Bluesky RunEngine [56].

A minor fraction of hot pixels (~0.1%) was masked to avoid recording substantial amounts of noise hits. This system allows for multihit functionality for each pixel, independent of others, along with a rapid readout bandwidth of 120 MPix/sec (30 MPix/sec/chip). Occasionally, photons excite charge in multiple adjacent pixels; to correct for this, a k-d tree algorithm was employed to cluster and centroid such events together. The 512 x 512 pixel array has two columns and two rows along the center (x and y = 255 and 256) of large, double-length (110 x 55 $\mu$m) interpixels. This was corrected by inserting rows and columns of two dummy pixels between the chips to preserve the correct physical distance between pixels.

We calibrated the ToT dependence on the X-ray energy by allowing the detection of beams of monochromatic scattered X-rays, varying their energy from 6 to 15 keV in 0.5 keV steps. We also cross-calibrated the ToT energy estimator using the spatial information of the selected SPDC pairs, which agreed well with the scattering calibrations. These two calibration techniques provide reliable and redundant ways to determine the X-ray energy, with the second approach only applicable for down-converted X-rays, but providing considerably more precise energy determination. The dual-calibration method ensures robust accuracy by leveraging spatial information as a complementary validation to the ToT measurements. These calibration studies identified pixel-by-pixel variations in the ToT response as a function of energy, which allowed for

the selection of cutoff values for the isolation of SPDC pairs on an individual pixel basis. These cutoff values were employed to reduce the high background of scattered 15 keV pump photons from the hits of lower energy (and thus lower ToT) SPDC single photons.

### *8.5. Imaging Samples*

The tungsten cat-shaped cutout and the E. cardamomum seed studied in the quantum correlation imaging setup were attached to a Kapton window via a quick drying epoxy. They were positioned in such a way to occlude the incident X-rays towards two of the adjacent Timepix3 sensors, which were considered to be the signal photon detectors. The other two ASICs were left unobstructed and were considered as idler photon detectors. The data presented in Fig. 1 and 3 represent 38 hours of collection.

### *8.6. Data Processing and Analysis*

All data processing and analysis were conducted using custom Python code, developed in-house and computed using CHX's local resources. This tailored approach facilitated meticulous processing of the raw Lynx T3 detector output, including hit clustering, distance corrections, data filtering, time coincidence searches, photon pair determinations, and analysis of spatial and energy correlations. Simulations were also performed using Python software.

## 9. Back matter

**Funding.** NSLS-II, a U.S. DOE Office of Science user facility at Brookhaven National Laboratory (BNL), is supported under contract DE-SC0012704. This project received support from the DOE-BER Bioimaging Science Program KP1607020 (BSSD), the DOE Office of Workforce Development for Teachers and Scientists (SULI), and the BNL Physics Department (SURP). Additional support came from the DOE QuantISED program and BNL LDRD grants 19-30 and 22-22.

**Acknowledgment.** We thank Bryan Marino and Rick Greene (NSLS-II Complex Scattering Support) for fabricating detector windows and beamstops and for beamline support; John Lara (NSLS-II Structural Biology Support) for crystal holders and goniometer hardware; Erik Muller (BNL Instrumentation) for providing the diamond crystal; Erik Hogenbirk and Erik Maddox (Amsterdam Scientific Instruments) for discussions on time/ToT resolution and Lynx T3 driver support; and Peter Schwander, Gabriel Beiner (U. Wisconsin Milwaukee), Andy Aquila, James Baxter, and Nick Hartley (SLAC LCLS-II) for helpful discussions.

**Disclosures.** The authors declare no conflicts of interest.

**Data availability.** Data underlying the results presented in this paper are not publicly available at this time but may be obtained from the authors upon reasonable request.

**Supplemental document.** See Supplement 1 for supporting content.

## References

1. A. Christ, A. Fedrizzi, H. Hübel, *et al.*, "Parametric down-conversion," in *Experimental Methods in the Physical Sciences,* vol. 45 (Elsevier, Amsterdam, 2013), pp. 351–410.
2. P. J. Mosley, J. S. Lundeen, B. J. Smith, *et al.*, "Heralded generation of ultrafast single photons in pure quantum states," Phys. Rev. Lett. **100**, 133601 (2008).
3. W. P. Grice, A. B. U'Ren, and I. A. Walmsley, "Eliminating frequency and space-time correlations in multiphoton states," Phys. Rev. A **64**, 063815 (2001).
4. B. Farella, G. Medwig, R. A. Abrahao, and A. Nomerotski, "Spectral characterization of an SPDC source with a fast broadband spectrometer," AIP Adv. **14**, 045034 (2024).
5. P. G. Kwiat, K. Mattle, H. Weinfurter, *et al.*, "New High-Intensity Source of Polarization-Entangled Photon Pairs," Phys. Rev. Lett. **75**, 4337 (1995).
6. M. Giustina, M. A. M. Versteegh, S. Wengerowsky, *et al.*, "Significant-Loophole-Free Test of Bell's Theorem with Entangled Photons," Phys. Rev. Lett. **115**, 250401 (2015).
7. L. K. Shalm, E. Meyer-Scott, B. G. Christensen, *et al.*, "Strong Loophole-Free Test of Local Realism," Phys. Rev. Lett. **115**, 250402 (2015).

8. A. Mair, A. Vaziri, G. Weihs, and A. Zeilinger, "Entanglement of the orbital angular momentum states of photons," Nature **412**, 313–316 (2001).
9. J. P. Dowling and G. J. Milburn, "Quantum technology: the second quantum revolution," Philos. Trans. Royal Soc. London. Ser. A: Math. Phys. Eng. Sci. **361**, 1655–1674 (2003).
10. J. L. O'Brien, G. J. Pryde, A. G. White, *et al.*, "Demonstration of an all-optical quantum controlled-NOT gate," Nature **426**, 264–267 (2003).
11. B. Ndagano, H. Defienne, D. Branford, *et al.*, "Quantum microscopy based on Hong-Ou-Mandel interference," Nat. Photonics **16**, 384–389 (2022).
12. T. B. Pittman, Y. H. Shih, D. V. Strekalov, and A. V. Sergienko, "Optical imaging by means of two-photon quantum entanglement," Phys. Rev. A **52**, R3429(R) (1995).
13. G. Harder, V. Ansari, B. Brecht, *et al.*, "An optimized photon pair source for quantum circuits," Opt. Express **21**, 13975–13985 (2013).
14. P.-A. Moreau, E. Toninelli, T. Gregory, and M. J. Padgett, "Imaging with quantum states of light," Nat. Rev. Phys. **1**, 367–380 (2019).
15. B. Levine and I. Freund, "Parametric down conversion of X-rays," Opt. Commun. **1**, 419–422 (1970).
16. P. Eisenberger and S. L. McCall, "X-ray Parametric Conversion," Phys. Rev. Lett. **26**, 684 (1971).
17. I. Freund and B. F. Levine, "Parametric Conversion of X Rays," Phys. Rev. Lett. **23**, 854 (1969).
18. Y. Yoda, T. Suzuki, X.-W. Zhang, *et al.*, "X-ray parametric scattering by a diamond crystal," J. Synchrotron Radiat. **5**, 980–982 (1998).
19. B. Adams, P. Fernandez, W.-K. Lee, *et al.*, "Parametric down conversion of X-ray photons," J. Synchrotron Radiat. **7**, 81–88 (2000).
20. B. Adams, Y. Nishino, D. Novikov, *et al.*, "Parametric down conversion of X-rays, recent experiments," Nucl. Instruments Methods Phys. Res. Sect. A: Accel. Spectrometers, Detect. Assoc. Equip. **467-468**, 1019–1020 (2001).
21. B. Adams, C. Buth, S. M. Cavaletto, *et al.*, "X-ray quantum optics," J. Mod. Opt. **60**, 2–21 (2013).
22. S. Sofer, O. Sefi, E. Strizhevsky, *et al.*, "Observation of strong nonlinear interactions in parametric down-conversion of X-rays into ultraviolet radiation," Nat. Commun. **10** (2019).
23. Z. Li, N. Medvedev, H. N. Chapman, and Y. Shih, "Radiation damage free ghost diffraction with atomic resolution," J. Phys. B: At. Mol. Opt. Phys. **51**, 025503 (2017).
24. A. Schori, C. Bömer, D. Borodin, *et al.*, "Parametric Down-Conversion of X Rays into the Optical Regime," Phys. Rev. Lett. **119** (2017).
25. A. Schori, D. Borodin, K. Tamasaku, and S. Shwartz, "Ghost imaging with paired x-ray photons," Phys. Rev. A (Coll. Park. **97** (2018).
26. S. Shwartz, R. N. Coffee, J. M. Feldkamp, *et al.*, "X-ray Parametric Down-Conversion in the Langevin Regime," Phys. Rev. Lett. **109**, 013602 (2012).
27. N. Hartley, D. Hodge, T. Buckway, *et al.*, "Confirming X-ray parametric down conversion by time–energy correlation," Results Phys. **57**, 107328 (2024).
28. L. J. Wong and I. Kaminer, "Prospects in x-ray science emerging from quantum optics and nanomaterials," Appl. Phys. Lett. **119** (2021).
29. D. Borodin, A. Schori, F. Zontone, and S. Shwartz, "X-ray photon pairs with highly suppressed background," Phys. Rev. A **94**, 013843 (2016).
30. N. J. Hartley, J. Baxter, S. Curtis, *et al.*, "X-ray parametric down-conversion at an XFEL," Optica **12**, 961–967 (2025).
31. S. Sofer, E. Strizhevsky, A. Schori, *et al.*, "Quantum enhanced x-ray detection," Phys. Rev. X **9**, 031033 (2019).
32. Q. Shen, I. Bazarov, and P. Thibault, "Diffractive imaging of nonperiodic materials with future coherent x-ray sources," J. synchrotron radiation **11**, 432–438 (2004).
33. E. F. Garman and M. Weik, "X-ray radiation damage to biological samples: recent progress," J. Synchrotron Radiat. **26**, 907–911 (2019).
34. S. Lloyd, "Enhanced Sensitivity of Photodetection via Quantum Illumination," Science **321**, 1463–1465 (2008).
35. C. L. Degen, F. Reinhard, and P. Cappellaro, "Quantum sensing," Rev. modern physics **89**, 035002 (2017).
36. S. Pirandola, B. R. Bardhan, T. Gehring, *et al.*, "Advances in photonic quantum sensing," Nat. Photonics **12**, 724–733 (2018).
37. M. D'Angelo and Y. Shih, "Quantum imaging," Laser Phys. Lett. **2**, 567 (2005).
38. J. H. Shapiro and R. W. Boyd, "The physics of ghost imaging," Quantum Inf. Process. **11**, 949–993 (2012).
39. G. Brida, M. Genovese, and I. Ruo Berchera, "Experimental realization of sub-shot-noise quantum imaging," Nat. Photonics **4**, 227–230 (2010).
40. C. A. Casacio, L. S. Madsen, A. Terrasson, *et al.*, "Quantum-enhanced nonlinear microscopy," Nature **594**, 201–206 (2021).
41. G. B. Lemos, V. Borish, G. D. Cole, *et al.*, "Quantum imaging with undetected photons," Nature **512**, 409–412 (2014).
42. M. Tsang, R. Nair, and X.-M. Lu, "Quantum Theory of Superresolution for Two Incoherent Optical Point Sources," Phys. Rev. X **6**, 031033 (2016).
43. M. Paúr, B. Stoklasa, Z. Hradil, *et al.*, "Achieving the ultimate optical resolution," Optica **3**, 1144–1147 (2016).
44. E. Brambilla, L. Caspani, O. Jedrkiewicz, *et al.*, "High-sensitivity imaging with multi-mode twin beams," Phys. Rev. A: At. Mol. Opt. Phys. **77**, 053807 (2008).

45. P. Espoukeh, G. Biener, J. Baxter, *et al.*, "Advancing X-ray quantum imaging through Monte-Carlo simulations," Sci. Reports **15**, 25359 (2025).
46. F. M. Pitters, N. Alipour Tehrani, D. Dannheim, *et al.*, "Time and Energy Calibration of Timepix3 Assemblies with Thin Silicon Sensors," (2018).
47. A. Zhao, M. van Beuzekom, B. Bouwens, *et al.*, "Coincidence velocity map imaging using Tpx3Cam, a time stamping optical camera with 1.5 ns timing resolution," Rev. Sci. Instruments **88** (2017).
48. J. C. Goodrich, R. Mahon, J. Hanrahan, *et al.*, "Imaging of x-ray pairs in a spontaneous parametric down-conversion process," arXiv preprint arXiv:2310.13078 (2023).
49. X. Llopart, "Timepix4: Specs & Plans," https://indico.cern.ch/event/591299/contributions/2423187/attachments/1393307/2123191/Timepix4_specs.pdf. Accessed: 2024-11-25.
50. Element Six, "Synthetic diamond and tungsten carbide experts," (2023). Accessed: 2023-08-24.
51. K. J. Gofron, "Using TimePix3 Detector for Neutron and X-Ray Studies," 32nd Linear Accel. Conf. (LINAC2024) pp. 725–727 (2024).
52. T. Poikela *et al.*, "Timepix3: a 65K channel hybrid pixel readout chip with simultaneous toa/tot and sparse readout," J. Instrum. **9**, C05013 (2014).
53. M. L. Rivers *et al.*, "areaDetector: EPICS software for 2-D detectors," in *Proc. 16th Int. Conf. on Accelerator and Large Experimental Control Systems (ICALEPCS'17),* (2018), pp. 1245–1251.
54. K. J. Gofron, "ADTimePix3," (2023). GitHub repository.
55. K. J. Gofron, B. Vacaliuc, J. Wlodek, *et al.*, "Deployment of ADTimePix3 areaDetector Driver at Neutron and X-Ray Facilities," 19th Int. Conf. Accel. Large Experpimental Physiscs Control. Syst. pp. 90–94 (2023).
56. D. Allan, T. Caswell, S. Campbell, and M. Rakitin, "Bluesky's Ahead: A Multi-Facility Collaboration for an a la Carte Software Project for Data Acquisition and Management," Synchrotron Radiat. News **32**, 19–22 (2019).